Clathrate formation in the Ba-Pd-Ge system: Phase equilibria, crystal structure, and physical properties

N. Melnychenko-Koblyuk, A. Grytsiv, P. Rogl, and M. Rotter
Institute of Physical Chemistry, University of Vienna, A-1090 Wien, Austria

E. Bauer, G. Durand, H. Kaldarar, R. Lackner, H. Michor, and E. Royanian
Institute of Solid State Physics, Vienna University of Technology, A-1040 Wien, Austria

M. Koza
Institut Laue Langevin, 6 rue Jules Horowitz, 38042 Grenoble, France

G. Giester
Institute of Mineralogy and Crystallography, University of Vienna, Althanstrasse 14, A-1090 Wien, Austria
(Received 6 May 2007; published 31 October 2007)

Phase relations at subsolidus temperatures as well as at $T=800\,^{\circ}C$, crystallographic data, electrical and thermal transport measurements, and heat capacity data are reported for several compositions within the clathrate type-I solid solution: $Ba_8Pd_xGe_{46-x-y}\square_y$ ($\square$ is a vacancy). The solid solution derives from binary clathrate $Ba_8Ge_{43}\square_3$ with a solubility limit of 3.8 Pd atoms per formula unit at $T=800\,^{\circ}C$. Structural investigations throughout the homogeneity region confirm cubic primitive symmetry consistent with the space group type $Pm\bar{3}n$ and lattice parameters ranging from $a=1.0657(2)$ nm for $Ba_8Ge_{43}\square_3$ to $a=1.077\,41(2)$ nm for $Ba_8Pd_{3.8}Ge_{42.2}\square_{0.0}$. The primary field of clathrate crystallization has been elucidated from micrography and differential thermal analyses. Both heat capacity and inelastic neutron diffraction define a low-lying, almost localized, phonon branch. Studies of transport properties evidence electrons as the majority charge carriers for most of the homogeneity region; however, at the Pd-rich limit, holes dominate the electronic transport. The crossover between both regimes provides appropriate conditions for attractively high Seebeck values. The lattice contribution dominates the overall thermal conductivity.

DOI: 10.1103/PhysRevB.76.144118 PACS number(s): 82.75.−z, 61.66.Fn, 72.15.Eb, 65.40.Ba

I. INTRODUCTION

In recent papers[1,2] we have dealt with the physical properties of Zn- and Cd-containing clathrate systems and have demonstrated that increasing Zn and Cd content drives the metallic system towards a metal-to-insulator transition, yielding interesting thermoelectric features. The present paper continues our systematic investigation of ternary clathrate phases $Ba_8Pd_xGe_{46-x-y}\square_y$ and $Ba_6M_xGe_{25-x}$, where *d* and *p* elements *M* are used for stabilization of the framework structure as well as for proper adjustment of the electronic density of states at the Fermi level. In a simple approach the Zintl concept may be exploited to track semiconducting behavior in clathrates: binary $Ba_8Ge_{43}\square_3$ with three framework defects[3,4] can be formulated as $[Ba^{+2}]_8[Ge^0]_{43}[\square^{-4}]_3$, yielding a surplus of four "conduction electrons" per formula unit. Consequently, void filling, substitution, and/or doping offer fruitful tools to tune the charge carrier concentration of clathrates in an optimal manner to tailor the highest possible thermoelectric performance. So far, only limited information is available on the thermoelectric performance of clathrates stabilized by platinum metals, such as Pd or Pt: the formation and crystal structure of type-I clathrates $Ba_8M_xGe_{46-x}$ (M=Pd,Pt, $x\sim 6$) have been investigated,[5] but no link was made to the binary clathrates Ba_6Ge_{25} (Ref. 6) and $Ba_8Ge_{43}\square_3$ (Refs. 3 and 4). Therefore the main goals of the present work are (a) to establish the extension of single-phase clathrate regions in the ternary system Ba-Pd-Ge, (b) to elucidate details of the crystal structure of clathrate type I, (c) to construct the phase diagram in the Ba-Pd-Ge system at $T=800\,^{\circ}C$, and (d) to define the physical (transport) properties of these ternary clathrates.

II. EXPERIMENT

Alloys with a weight of 1–2 g were prepared by arc-melting (weight loss less than 0.1%) on a water-cooled copper hearth in Ti-gettered argon from elemental ingots with a purity better than 99.9 wt %. The alloys were sealed in evacuated quartz tubes and annealed at $T=800\,^{\circ}C$ for 7 days before quenching in water. Phase diagram studies, characterization of composition via light optical and scanning electron microscopy (LOM and SEM), electron probe microanalysis (EPMA calibrated against binary clathrate Ba_8Ge_{43}, PdGe and ternary τ_1 as standards), x-ray structure determinations and refinements on powders (XRPD) as well as on a single crystal (XRSD) of $Ba_8Pd_{3.7}Ge_{42.3}$ were carried out with a series of standard techniques described in Refs. 1 and 2. Isothermal reaction temperatures were derived from thermal arrests determined in a calibrated Netzsch STA 409 PG/4/G Luxx differential scanning calorimeter (DSC) employing a heating rate of 5 K/min in closed Al_2O_3 crucibles under argon (neither vapor losses nor reaction with crucible walls detected). Physical property measurements on single-phase polycrystalline material comprise heat capacity, optical measurements, as well as electronic and thermal transport. De-

TABLE I. Composition and crystallographic data for $Ba_8Pd_xGe_{46-x-y}\square_y$. Data are standardized according to Typix (Ref. 11).

Nominal composition	EPMA (at. %)[a] Ba	Pd	Ge	Accepted composition[b,c]	Lattice Parameter a (nm)	Ge(2) in 16*i* (x,x,x)	Ge(3) in 24*k* $(0,y,z)$
Ba_8Ge_{43}	15.7	0.0	84.3	$Ba_8Ge_{43}\square_3$	1.0657(2)		
$Ba_8Pd_2Ge_{44}$	15.3	3.9	80.8	$Ba_8Pd_{2.0}Ge_{42.5}\square_{1.5}$	1.07175(2)	0.18312(8)	0.12016(1), 0.31575(11)
$Ba_8Pd_3Ge_{43}$	15.2	5.5	79.3	$Ba_8Pd_{2.9}Ge_{42.6}\square_{0.5}$	1.07560(2)	0.18290(5)	0.12012(7), 0.31295(7)
$Ba_8Pd_{3.5}Ge_{42.5}$	15.4	6.3	78.3	$Ba_8Pd_{3.3}Ge_{42.5}\square_{0.2}$	1.07679(1)	0.18312(8)	0.11982(11), 0.31250(12)
$Ba_8Pd_{3.75}Ge_{42.25}$	15.3	6.7	78.0	$Ba_8Pd_{3.6}Ge_{42.0}\square_{0.4}$	1.07760(3)	0.18237(8)	0.11980(12), 0.31173(11)
$Ba_8Pd_4Ge_{42}$	15.3	7.1	77.6	$Ba_8Pd_{3.7}Ge_{42.3}\square_{0.0}$	1.07743(2)	0.18249(9)	0.11999(13), 0.31327(12)
				$Ba_8Pd_{3.8}Ge_{42.2}\square_{0.0}$[d]	1.0774(2)	0.18344(3)	0.11969(5), 0.31222(6)
$Ba_8Pd_4Ge_{42}$	15.3	7.3	77.4	$Ba_8Pd_{3.8}Ge_{42.2}\square_{0.0}$	1.07710(2)	0.18339(11)	0.11966(16), 0.31193(16)
$Ba_8Pd_{4.25}Ge_{41.75}$	15.3	7.3	77.4	$Ba_8Pd_{3.81}Ge_{42.19}\square_{0.0}$	1.07741(2)	0.18362(7)	0.11952(12), 0.31127(10)
$Ba_8Pd_{4.5}Ge_{41.5}$	15.2	7.2	77.6	$Ba_8Pd_{3.82}Ge_{42.18}\square_{0.0}$	1.07747(2)	0.18311(17)	0.11983(10), 0.31133(11)

[a]After calibration against system internal standards; standard deviations $\leqslant$0.3 at. % Pd.
[b]Ba sublattice (2*a* and 6*c* sites) was found to be complete.
[c]Formula from EMPA+Rietveld refinement.
[d]X-ray single-crystal data at 300 K; $R_{F^2}=0.029$, GOF=1.082.

tails are given in Refs. 1 and 2. The Hall coefficient R_H was determined using the van der Pauw method[7] in the context of a procedure recommended by NIST.[8] Inelastic neutron scattering (INS) data were collected on the time-of-flight spectrometer IN6 at the Institute Laue Langevin in Grenoble, France, with an incident neutron wavelength of 0.41 nm in the extreme time-focusing mode, offering an energy resolution of 0.15 meV in the energy range up to 12 meV.

III. RESULTS AND DISCUSSION

A. Phase equilibria in the Ge-PdGe-$BaGe_2$ region of the Ba-Pd-Ge system

In order to determine the full range of the ternary clathrate type-I solution extending from binary $Ba_8Ge_{43}\square_3$, alloys with nominal composition $Ba_8Pd_xGe_{46-x}$ $(0\leqslant x\leqslant 10)$ annealed at $T=800$ °C were examined by means of XRPD, LOM, and EPMA (precisely calibrated against binary and ternary standards). X-ray microanalyses reveal a decrease of the Ba content with increasing Ge and Pd substitution, which is associated with a change of the amount of vacancies in the crystal lattice (see Table I). The deficiency of the structure was calculated from EPMA data adopting a complete Ba sublattice (full occupancy of Ba in 2*a* and 6*c* sites, as proven from x-ray refinements). The resulting maximal solubility of 7.3 at. % Pd at $T=800$ °C in type-I clathrate corresponds to 3.8 Pd atoms per unit cell. In accordance with the difference of atomic radii of the elements the clathrate unit cell expands with increasing Pd content (Fig. 1). The sample $Ba_8Pd_4Ge_{42}$ (nominal composition) is a single-phase clathrate with lattice parameter $a=1.077\,43(2)$ nm, but a ternary alloy with higher palladium content, $Ba_8Pd_6Ge_{40}$, was found to be multiphase with a similar lattice parameter [$a=1.077\,21(2)$ nm] for the clathrate phase. These values are close to the one reported by Ref. 5 for a clathrate composition "$Ba_8(Pd,Ge)_6Ge_{40}$" (Fig. 1).

As the binary clathrate Ba_8Ge_{43} only exists in a small temperature region from 770 to 810 °C,[4] it was interesting to test the stability range of ternary $Ba_8Pd_xGe_{46-x-y}\square_y$ at lower temperatures. Indeed, annealing the sample with nominal composition $Ba_8Pd_6Ge_{40}$ at $T=700$ °C for 10 days and subsequently at $T=500$ °C for 150 days in both cases confirmed the existence of type-I clathrate with composition and lattice parameters close to those obtained from the sample annealed at $T=800$ °C.

To evaluate the equilibria between clathrate type I (κ_I) and type IX (Ba_6Ge_{25}, κ_{IX}) we have prepared the alloy Ba_6PdGe_{24}. However, samples in as-cast and annealed states ($T=800$ °C) decompose quickly due to the presence of moisture-sensitive $BaGe_2$. XRPD of specimens, washed in diluted H_2SO_4 to remove decomposition products, showed

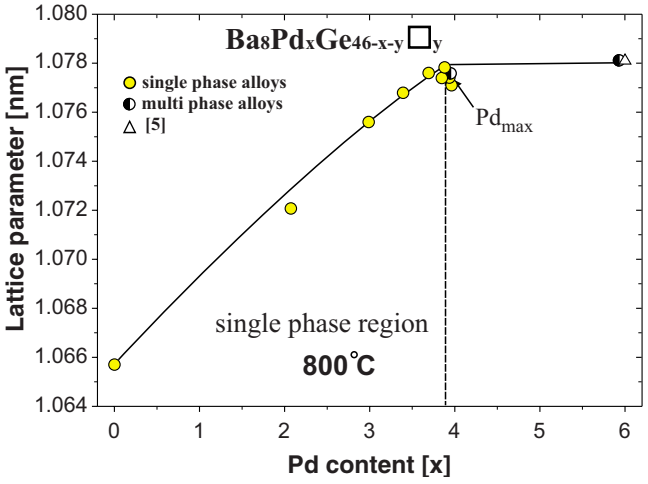

FIG. 1. (Color online) Lattice parameters vs Pd content for $Ba_8Pd_xGe_{46-x-y}\square_y$ alloys. The dashed line denotes the solubility limit of Pd at $T=800$ °C.

that the residual powder consists of type-I clathrate with lattice parameter $a=1.073\,14(1)$ nm practically unchanged with respect to the nonwashed original powder [$a=1.0733(3)$ nm]. Employing the lattice parameter versus composition curve we arrive at a Pd content of 2.3 Pd atoms per unit cell (Fig. 1). As no type-IX clathrate was detected by XRPD, the solubility of Pd in type-IX clathrate is below 1 atom Pd per unit cell.

During the investigation of phase equilibria a new ternary compound τ_1 with composition $BaPdGe_3$ [$BaNiSn_3$ type, $a=0.455\,08(2)$ and $c=1.0365(1)$ nm] was found. Details of the crystal structure and physical properties are subject of a forthcoming publication.[9] From the available data on the constitution of as-cast and annealed alloys, phase equilibria were determined covering the regions of existence as well as the solidification behavior of both clathrate phases. Phase relations are presented as a partial liquidus projection, a partial isothermal section at $T=800$ °C, a solidus projection, and a partial reaction scheme for the region Ge-PdGe-$BaGe_2$ (Fig. 2). Ternary phase relations were combined with the binary diagram Ba-Ge from Ref. 4 and Pd-Ge from Ref. 10. It has to be noted that at $T=800$ °C some alloys are in equilibrium with a liquid phase that covers a significant part of the isothermal section [Fig. 2(a)]. The phase composition and state of the alloys after anneal at $T=700$ °C were used to define the equilibria at subsolidus temperatures [Fig. 2(c)].

Alloys $Ba_6Pd_3Ge_{22}$ in as-cast and annealed states decompose in air due to the presence of $BaGe_2$. Besides decomposition products, the specimens contain κ_I (type-I clathrate) and the τ_1 phase. The composition of clathrate κ_I, as determined from the lattice parameter (Fig. 1), is close to the maximal solubility of Pd in κ_I. The as-cast sample $Ba_8Pd_6Ge_{40}$ does not contain $BaGe_2$ but shows τ_1 as the primary phase. Therefore the separation line between the primary crystallization fields of $BaGe_2$ and τ_1 lies between compositions $Ba_6Pd_3Ge_{22}$ and $Ba_8Pd_6Ge_{40}$ [Fig. 2(a)]. As the decomposition of $BaGe_2$-containing alloys limits the characterization of these samples, the liquidus surface and reaction scheme for the region close to $BaGe_2$ [Figs. 2(a) and 2(b)] are tentative.

Alloy $Ba_8Pd_6Ge_{40}$ annealed at $T=800$ °C for 7 days contains huge grains of τ_1 ($BaPdGe_3$) and κ_I (type-I clathrate) that were grown in equilibrium with liquid [Fig. 3(a)]. During quenching from $T=800$ °C this liquid crystallizes in form of a ternary eutectic [E, 719 ± 3 °C: $L \Leftrightarrow \tau_1+(\mathrm{Ge})+\mathrm{PdGe}$; Fig. 3(b)] with composition $Ba_{2.3}Pd_{27.6}Ge_{70.1}$. No PdGe phase was detected in this alloy after anneal at $T=700$ °C: the sample consists of τ_1, κ_I, and (Ge). Alloy $Ba_{17}Pd_{19}Ge_{64}$ annealed at $T=800$ °C is almost single phase τ_1 [Fig. 3(c)] with small amounts of κ_I and (Ge) that were formed during monovariant crystallization $L \Rightarrow \kappa_I+(\mathrm{Ge})$. During anneal at $T=700$ °C clathrate κ_I decomposes [Fig. 3(d)] and the sample contains PdGe, τ_1, and (Ge). The microstructure of as-cast alloy $Ba_8Pd_{22}Ge_{70}$ represents the crystallization of liquid along the monovariant line $L \Rightarrow \tau_1+(\mathrm{Ge})$ [coarse eutectic; see Fig. 4(a)], and the formation of fine grains of PdGe in the invariant point E. This alloy was completely melted at $T=800$ °C, and therefore shows a microstructure [Fig. 4(b)] that is very similar to the as-cast state

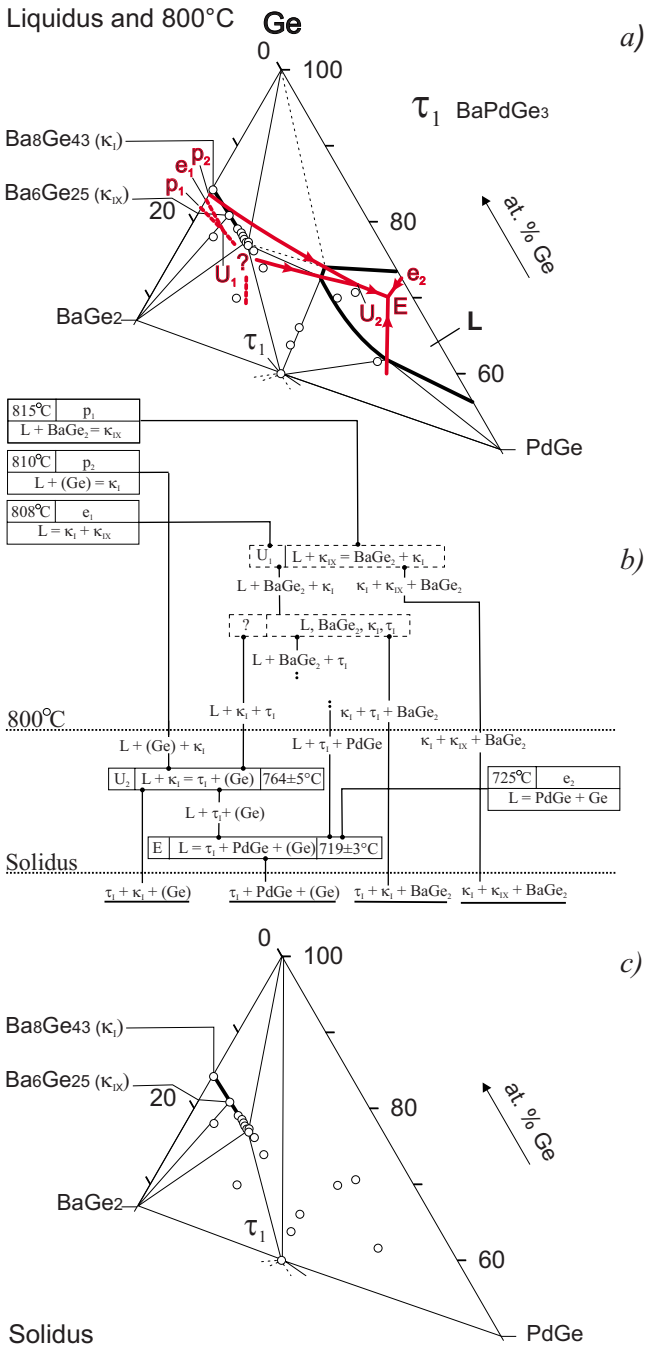

FIG. 2. (Color online) Partial liquidous surface and isothermal section at $T=800$ °C (a), partial reaction scheme (b), and solidus (c) of the Ba-Pd-Ge ternary system in the region Ge-PdGe-$BaGe_2$.

[Fig. 4(a)]. Concerning the crystallization data of alloys $Ba_8Pd_6Ge_{40}$, $Ba_{17}Pd_{19}Ge_{64}$ and $Ba_8Pd_{22}Ge_{70}$, we derive the existence of an invariant equilibrium U_2, 764 ± 5 °C: $L+\kappa_I \Leftrightarrow \tau_1+(\mathrm{Ge})$. The composition of alloy $Ba_8Pd_{30}Ge_{62}$ lies close to the line of joint crystallization of τ_1 and PdGe. The microstructure of as-cast alloys presents a small quantity of primary grains of τ_1 [Fig. 4(c)] and a mixture of two eutectics [Fig. 4(d)]: monovariant ($\tau_1+\mathrm{PdGe}$, coarse structure) and invariant [E, $\tau_1+\mathrm{PdGe}+(\mathrm{Ge})$, fine structure]. Annealing of this specimen at $T=800$ °C results in the formation of

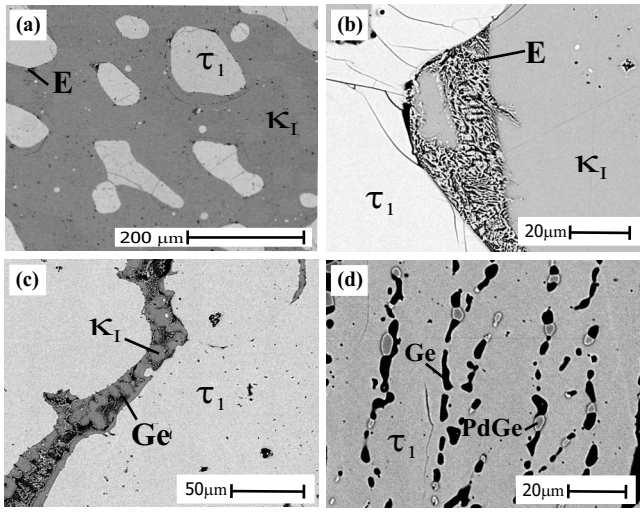

FIG. 3. Microstructures of $Ba_8Pd_6Ge_{40}$, (a) as-cast, (b) $T=800$ °C, and $Ba_{17}Pd_{19}Ge_{64}$, (c) $T=800$ °C, (d) $T=700$ °C, alloys.

large crystals of τ_1 [Fig. 4(e)] and in a coarse eutecticlike structure [Fig. 4(f)] that forms during crystallization of liquid along the monovariant line $L \Rightarrow \tau_1 + \mathrm{PdGe}$. The partial liquidus surface [Fig. 2(a)] shows that the type-I clathrate (κ_I) $Ba_8Pd_xGe_{46-x-y}\square_y$ has a much wider primary crystallization field than binary Ba_8Ge_{43}, which coexists in equilibrium with liquid only in a range of compositions of less than 1 at. % and only in a small temperature interval from 810 to 808 °C.[4] The primary crystallization field of type-I

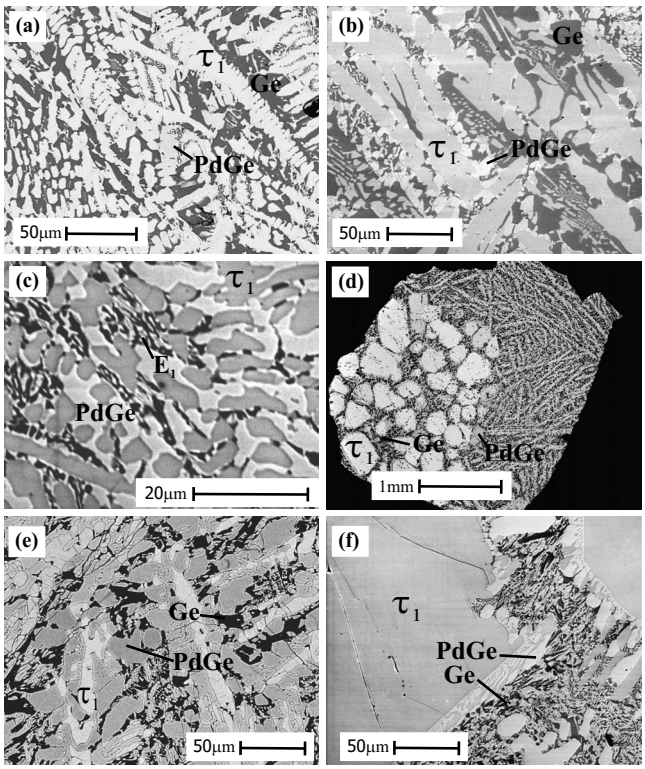

FIG. 4. Microstructures of alloys $Ba_8Pd_{22}Ge_{70}$, (a) as-cast, (b) 800 °C, $Ba_8Pd_{30}Ge_{62}$, (c) as-cast, and (d), (e), (f) $T=800$ °C.

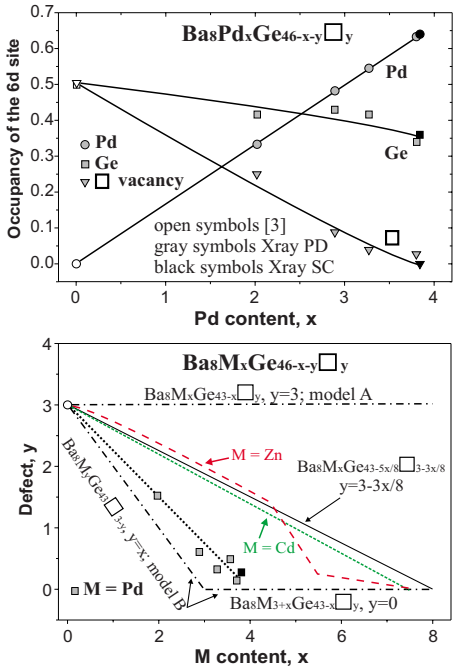

FIG. 5. (Color online) The 6*d* site preference for $Ba_8Pd_xGe_{46-x-y}\square_y$ (a) and (b) dependences of deficiency from *M* (*M*=Pd,Zn,Cd) content in $Ba_8Pd_xGe_{46-x-y}\square_y$ are compared for two boundary models for the incorporation of *M* atoms in the lattice of $Ba_8Ge_{43}\square_3$.

clathrate in the ternary system enlarges significantly from 810 to 764 °C.

B. Crystal chemistry of $Ba_8Pd_xGe_{46-x-y}\square_y$

In order to evaluate atom site preferences in $Ba_8Pd_xGe_{46-x-y}\square_y$, x-ray powder diffraction data from single-phase samples with $0 \leqslant x \leqslant 4 (y=0)$ were collected at room temperature. For a single crystal, selected from a sample with nominal composition $Ba_8Pd_4Ge_{42}$, x-ray intensity data were recorded at three temperatures: 100, 200, and 300 K. In all cases extinctions were consistent with a primitive cubic lattice (space group $Pm\bar{3}n$, $a \sim 1.1$ nm) and inferred isotypism with the structure of type-I clathrate. No extra reflections indicating a larger unit cell $a'=2a$ as reported by Ref. 4 were detected in the investigated crystals. The heavy barium atoms were unambiguously found in sites 2*a* (0, 0, 0) and 6*c* $\left(\frac{1}{4},0,\frac{1}{2}\right)$, while the electron density distribution for the remaining sites appeared as follows: (i) constant electron densities in both lattice sites 16*i* and 24*k* and (ii) an increasing number of electrons in the 6*d* site with increasing Pd content. Taking into account that the 6*d* site contains vacancies in binary Ba_8Ge_{43},[4] the refinement of occupancies for three species in one site (Ge and Pd atoms and vacancies) is not reliable. Therefore, the Pd content in the 6*d* site was fixed from the EPMA data, and refinement of the Ge content in this site allowed us to determine the number of vacancies (see Table I). The site preference shown in Fig. 5(a) reveals that the amount of germanium in the 6*d* site is almost constant while Pd atoms fill the vacancies in Ba_8Ge_{43}.

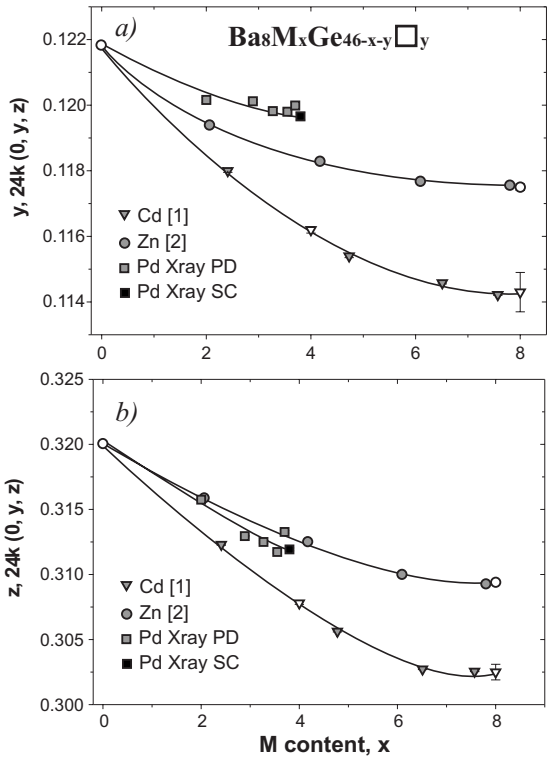

FIG. 6. Compositional dependence of positional parameters y (a) and z (b) for the Ge(3) site [$24k$ $(0,y,z)$ in $Ba_8Pd_xGe_{46-x-y}\square_y$ (M=Pd,Zn,Cd)]. Solid symbols, our data; open symbols, Refs. 3 and 12.

Finally, for 3.8 Pd atoms per unit cell (x=3.8), no vacancy was detected in the 6d site.

Such a scenario for the incorporation of Pd atoms in type-I clathrate is different from the mode observed for Cd and Zn atoms.[1,2] It is interesting to compare the amount of vacancies as a function of M content [M=Pd,Zn,Cd; see Fig. 5(b)] for two limit models of M atom incorporation in the lattice of $Ba_8Ge_{43}\square_3$. Model A corresponds to M and Ge substitution at a constant level of vacancies [three voids per formula as observed in binary $Ba_8Ge_{43}\square_3$ (Ref. 4)]. Accordingly the composition is described by formula $Ba_8M_xGe_{43-x}\square_3$. Model B suggests that M atoms at first enter the three empty lattice sites and only after completely filling these sites at x=3 do atoms M start to substitute for germanium adhering to the formula $Ba_8M_{3+x}Ge_{43-x}$. Experimental data for M=Cd (Ref. 1) and Zn (Ref. 2) clearly show a behavior intermediate between these two models; i.e. (Cd, Zn) atoms fill vacancies and simultaneously substitute for Ge atoms in the framework, while the incorporation of palladium atoms is close to model B. Compositions obtained from refinements of x-ray single-crystal and powder-diffraction data were found to be in fine agreement with EPMA data (see Table I).

The Ge and Pd substitution in the framework does not affect the 16i site, but a significant change is observed for the z coordinate of the Ge(3) atoms in the 24k site. The compositional change of the 24k site coordinate is compared with data obtained for Zn- and Cd-containing clathrates (Fig. 6). The change for the z coordinate [Fig. 6(b)] is in line with the difference of the atomic radii of the elements $r_{Cd}>r_{Pd}>r_{Zn}$, whereas the y coordinate [Fig. 6(a)] changes only slightly. The variation of the crystallographic parameters (lattice parameter, atomic coordinates, and site occupancy) with Pd content is also well reflected by a compositional dependence of the interatomic distances. Generally, distances monotonically increase following the trend observed for the lattice parameters (Fig. 1). It should be noted that XRPD and XRSC data show excellent agreement as a basis for the (i) marginal influence of profile parameters in Rietveld refinements and (ii) reliable dependences of atom parameters versus Pd composition derived from both techniques.

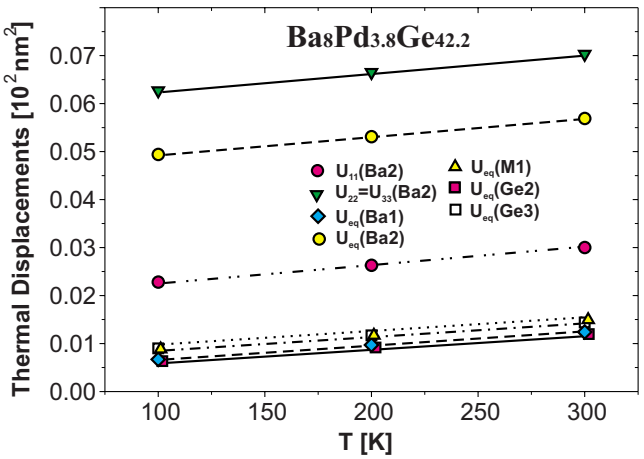

FIG. 7. (Color online) Thermal atom displacement parameters of $Ba_8Pd_{3.8}Ge_{42.2}$ vs temperature.

The atomic displacement parameters (ADPs) for Ba atoms located in the 6c site [Ba(2)] show a significant anisotropy in contrast to Ba(1) atoms, which exhibit normal temperature behavior (see Fig. 7) with a thermal expansion coefficient determined as $\alpha=1.1\times10^{-5}$ K^{-1}. If the $Ba_8Pd_{3.8}Ge_{42.2}$ crystal is considered as a simple Debye solid with Ba(2) atoms behaving like Einstein oscillators, the thermal displacements U_{ii} and the Einstein temperatures $\Theta_{E,ii}$ are related by

$$U_{ii}=\frac{\hbar^2}{2m_{Ba}k_B\theta_{E,ii}}\coth\left(\frac{\theta_{E,ii}}{2T}\right), \quad (1)$$

where m_{Ba} is the atomic mass of Ba. From the linear slope $\Delta U_{ii}/\Delta T$ in Fig. 7 the force constants K_{ii} [g s^{-1}], the frequency of vibrations ν_{ii} [10^{12} s^{-1}], and hence the Einstein temperatures $\theta_{E,ii}$ [K] can be extracted. Although from symmetry constraints U_{11} for Ba(2) atoms is different from $U_{22}=U_{33}$, the linear slopes $\Delta U_{ii}/\Delta T$ are indifferent for ADPs of all atoms yielding $\theta_{E,ii}$=95 K. It is interesting to note that Ba(1) atoms (spherical by symmetry) do not show a thermal displacement factor enhanced over general ADP values for framework atoms. Thus no special rattling effect can be derived for Ba(1) atoms.

C. Physical properties

1. Heat capacity

Temperature-dependent heat capacity measurements were carried out on $Ba_8Pd_{3.3}Ge_{42.5}\square_{0.2}$ and $Ba_8Pd_{3.82}Ge_{42.18}$ as

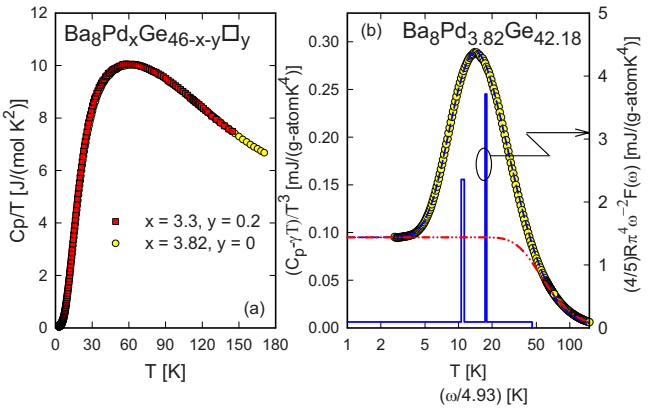

FIG. 8. (Color online) Temperature-dependent specific heat C_p of $Ba_8Pd_{3.3}Ge_{42.5}\square_{0.2}$ and $Ba_8Pd_{3.82}Ge_{42.18}$, plotted as C_p/T vs T (a) and $(C_p-\gamma T)/T^3$ vs ln T (b). The dashed line is a least-squares fit of the experimental data using the model described in the text with two Einstein-like modes (θ_D=226 K, ω_{EL1}=53.8 K with a width of 3.6 K and ω_{EL2}=86.6 K with a width of 3.5 K). The dash-double-dotted line is the simple Debye function with θ_D^{LT}=268 K, highlighting the substantial difference to the heat capacity observed. The solid lines (referring to the right axis) sketch the phonon spectral function $F(\omega)$ plotted as $\omega/4.93$ vs $(5/4)R\pi^4\omega^{-2}2F(\omega)$ for which ω is given in degrees Kelvin.

representatives of this family of clathrates. The results of these investigations are displayed in Figs. 8(a) and 8(b) as C_p/T vs T and as $(C_p-\gamma T)/T^3$ vs ln T for $Ba_8Pd_{3.82}Ge_{42.18}$. The latter representation can be used to visualize deviations of the lattice dynamics from that expected in terms of the simple Debye model. Obviously, $Ba_8Pd_{3.82}Ge_{42.18}$ does not follow the Debye model in the whole temperature range studied. The same holds for $Ba_8Pd_{3.3}Ge_{42.5}\square_{0.2}$, not shown in Fig. 8(b). Using only data below 4 K and applying a standard analysis of the specific heat of metals at low temperatures allows one to extract the Sommerfeld value γ and the low-temperature Debye temperature θ_D^{LT}. The electronic contributions γ to the specific heat for $Ba_8Pd_{3.3}Ge_{42.5}\square_{0.2}$ and $Ba_8Pd_{3.82}Ge_{42.18}$, respectively, are deduced as 15 and <0.05 mJ/(mol K^2), whereas θ_D^{LT} yields 260 and 268 K. The observed electronic contribution to the specific heat refers to distinctly different density of states (DOS) features around the Fermi energy E_F. While the former compound shows rather metalliclike behavior, the latter refers to a DOS almost vanishing at E_F and is thus placed next to a semiconducting region.

Significant deviations from the simple Debye model indicate a rather complicated phonon spectrum for this family of clathrates. The spectrum is supposed to be composed of background vibrations originating from the cagelike structure—represented by a Debye spectrum—and, additionally, from the rattling modes of the loosely bound electropositive Ba atoms. The latter should follow the behavior with Einstein-like frequencies. In order to qualitatively and quantitatively describe the lattice dynamics, we have adapted a model which incorporates some fine structure in the phonon density of states.[13,14] The latter is represented by a spectral function $F(\omega)$, allowing us to express the heat capacity as

$$C_{ph}(T) = 3R\int_0^\infty F(\omega)\frac{\left(\frac{\omega}{2T}\right)^2}{\sinh^2\left(\frac{\omega}{2T}\right)}d\omega, \qquad (2)$$

with ω the phonon frequency and R the gas constant. The most common assumptions on $F(\omega)$ are $F(\omega)=\delta(\omega)$ and $F(\omega)\sim\omega^2$ up to a cutoff frequency ω_D, corresponding to the well-known Einstein and Debye models, respectively. Junod *et al.*[13] demonstrated that certain functionals of the phonon specific heat take the form of convolutions of the phonon spectrum. In particular, $(5/4)R\pi^4C_{ph}T^3$ is an image of the spectrum $\omega^{-2}F(\omega)$ for $\omega=4.93T$, where ω is expressed in degrees Kelvin. Based on these considerations we have constructed an elementary phonon spectrum and have carried out least-squares fits to the data. In a first approximation we have assumed that besides a Debye density of states, the system is composed of two additional, energetically separated Einstein-like modes. Different to the standard Einstein model of the specific heat, a certain frequency width for each of these branches is allowed. The results of this procedure performed for $Ba_8Pd_{3.82}Ge_{42.18}$ are shown in Fig. 8(b). The overall goodness of the fit is extremely high, revealing a Debye temperature θ_D=226 K and two narrow structures at θ_{EL1}=53.8 K and θ_{EL2}=86.6 K, with corresponding spectral widths of 1.8 and 1.5 K, respectively. Accordingly, both contributions have different spectral weights. Based on this fit, the phonon spectrum is constructed and plotted in Fig. 8(b), referring to the right axis (solid line). The spectral weight follows from the constraint that for $T\to 0$ the height of the phonon density of states coincides with the value of C_p/T^3 for $T\to 0$. Very similar figures are derived for $Ba_8Pd_{3.3}Ge_{42.5}\square_{0.2}$ (not shown here), in good agreement with data observed for Ba-Cd-Ge (Ref. 1) and Ba-Zn-Ge (Ref. 2) clathrates. Moreover, other cage-forming compounds like skutterudites have been found with similar widths of Einstein-like modes.[15]

As already discussed above, such localized lattice vibrations are also inferred from our XRD analysis of the anisotropic thermal displacement factor of Ba(2), yielding an overall Einstein temperature of 95 K, while for Ba(1) no enhanced vibrational modes were observed.

2. Neutron spectroscopy and the generalized density of states

To substantiate the conclusions drawn from heat capacity experiments we have performed neutron inelastic scattering measurements on a $Ba_8Pd_{3.8}Ge_{42.2}$ sample. The application of cold neutrons—i.e., neutrons with energies of some few meV (5–50 K)—for spectroscopy studies is a powerful experimental approach to shed light on the vibrational properties of a substance. The kinematic properties of cold neutrons match the energy and the momentum distributions of vibrational excitations. Hence, cold neutrons are highly sensitive probes for establishing the energies of Einstein modes in the meV energy range.

Figure 9(a) reports the generalized density of states $G(\omega)$ of $Ba_8Pd_{3.8}Ge_{42.2}$ in comparison with $G(\omega)$ of $Ba_8Zn_{7.7}Ge_{38.3}$ presented in detail in Ref. 2. A corresponding data treatment

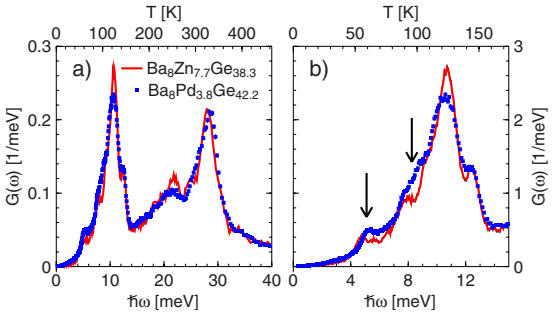

FIG. 9. (Color online) (a) Generalized density of states $G(\omega)$ of $Ba_8Pd_{3.8}Ge_{42.2}$ compared with $G(\omega)$ of $Ba_8Zn_{7.7}Ge_{38.3}$. (b) Close-up of the low-energy part of $G(\omega)$ determining substantially the properties of the specific heat of the samples. Vertical arrows indicate the increase of Einstein-mode energies and an intensity enhancement found in the $Ba_8Pd_{3.8}Ge_{42.2}$ sample.

has been pursued for both samples whereby $G(\omega)$ of $Ba_8Zn_{7.7}Ge_{38.3}$ is taken as a reference being normalized to three modes in the energy range up to 32 meV. The weighed neutron scattering power of the $Ba_8Pd_{3.8}Ge_{42.2}$ sample, which is by about 3% higher than the one of $Ba_8Zn_{7.7}Ge_{38.3}$, has been taken into account when its $G(\omega)$ is computed.

As a rough characterization of the inelastic response we may conclude that both density of states show identical features. This holds for the three strong maxima at about 10.5 meV (125 K), 22 meV (250 K), and 28 meV (325 K) as well as for the structures appearing as small peaks and shoulders at the strong maxima. However, a detailed inspection of the structures reveals substantial differences which are in agreement with the heat capacity measurements. For this reason let us restrict the discussion to the features at the strong maximum around 10 meV since they determine essentially the specific heat characteristics of the samples. For better visibility this region is shown in an enlarged presentation in Fig. 9(b). It can be easily concluded from Fig. 9(b) that the intensity at this maximum is subject to a redistribution when changing the sample composition. The Pd-substituted sample reveals a reduction of intensity at the central peak in favour of the intensity of the side peaks. In particular the number of vibrational modes is strongly enhanced in the energy range 7.5–9 meV (85–100 K). Moreover, the Einstein mode of the lowest energy is shifted by 0.5 meV (6 K) from 4.7 meV (55 K) in $Ba_8Zn_{7.7}Ge_{38.3}$ to 5.2 meV (60 K) in $Ba_8Pd_{3.8}Ge_{42.2}$.

We recall that the analysis of the specific heat properties in terms of Einstein oscillators resulted in two modes centered at $\Theta_{EL1} \approx 48.4$ K and $\Theta_{EL2} \approx 84.8$ K in $Ba_8Zn_{7.7}Ge_{38.3}$ and at $\Theta_{EL1} \approx 53.8$ K and $\Theta_{EL2} \approx 86.6$ K in $Ba_8Pd_{3.8}Ge_{42.2}$. Consequently both features—the shift of the low-energy Einstein mode and the mode enhancement at about 8 meV (90 K) in the neutron scattering data—reflect the mode shifts concluded from specific heat experiments.

Referring to the classical theory of lattice vibrations[16] we may find a simple but conclusive explanation for the intensity redistribution at the first strong maximum. The density of states of both samples is dominated in the low-energy region by the vibrations of the Ba atoms.[2] This is due to the energy dependence $\hbar\omega$ upon the mass M—i.e., $\hbar\omega \sim 1/\sqrt{M}$. Hence, the relatively high mass of 137.3 amu makes low-energy eigenfrequencies preferential for Ba when compared with the light Ge atoms (72.6 amu) of the host lattice. Substituting Ge by other elements the coupling efficiency of the substitute with Ba and Ge and thus the effect on the characteristic energies of Ba and Ge depend on the mass of the substitute. As a consequence we may expect Pd (M =106.4 amu) to couple with Ba more efficiently than Zn (M=65.4 amu) and to provoke a renormalization of the Ba eigenmodes in favor of a higher energy as given by the Pd eigenmode energies.

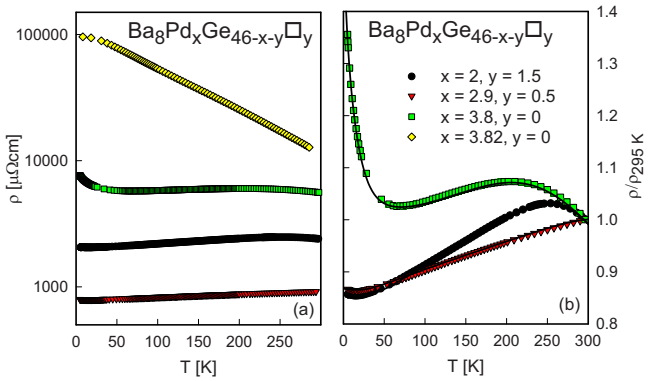

FIG. 10. (Color online) (a) Temperature-dependent resistivity ρ of various concentrations of $Ba_8Pd_xGe_{46-x-y}\square_y$. (b) Normalized resistivity of $Ba_8Pd_xGe_{46-x-y}\square_y$. The solid lines are least-squares fits as explained in the text.

3. *Temperature-dependent electronic and thermal transport*

The series of $Ba_8Pd_xGe_{46-x-y}\square_y$ provides the possibility to study the evolution of electronic transport in clathrates due to a tuning of the charge carrier density originating from the Ge and Pd substitution as well as by the change of the vacancy density. This enables us to drive systems close to a metal-to-insulator transition where large thermopower values are expected.

The results of the present resistivity study on various concentrations of $Ba_8Pd_xGe_{46-x-y}\square_y$ are displayed in Figs. 10(a) and 10(b). Data in Fig. 10(a) are plotted on a logarithmic resistivity scale in order to get rid of the large variation of the absolute resistivity values. Obviously, the temperature-dependent resistivity $\rho(T)$ changes from a metallicklike behavior for smaller Pd concentrations to a semiconducting one (for the whole temperature range studied) for the compound containing 3.82 Pd. The semiconducting behavior of the latter compound is in excellent agreement with the observation that the Sommerfeld value of the specific heat, $\gamma < 0.05$ mJ/(mol K^2), refers to a vanishing density of states right at the Fermi energy.

In order to understand the nonmonotonous variation of the absolute resistivity, we have carried out Hall measurements at low temperatures. As an example, the charge carrier density n and mobility μ of $Ba_8Pd_xGe_{46-x-y}\square_y$, x=3.6 and y =0.4, are plotted in Fig. 11 as a function of temperature (a) and magnetic field (b).

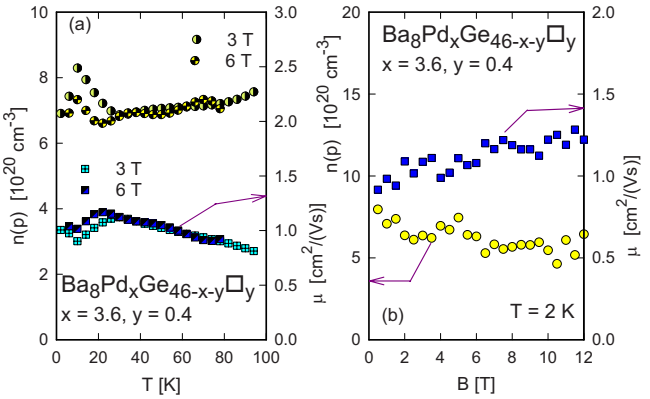

FIG. 11. (Color online) (a) Temperature-dependent charge carrier density n and mobility μ for $Ba_8Pd_xGe_{46-x-y}\square_y$, $x=3.6$ and $y=0.4$, taken at 3 and 6 T. (b) Field-dependent charge carrier density n and mobility μ for $Ba_8Pd_xGe_{46-x-y}\square_y$, $x=3.6$ and $y=0.4$ taken at 2 K.

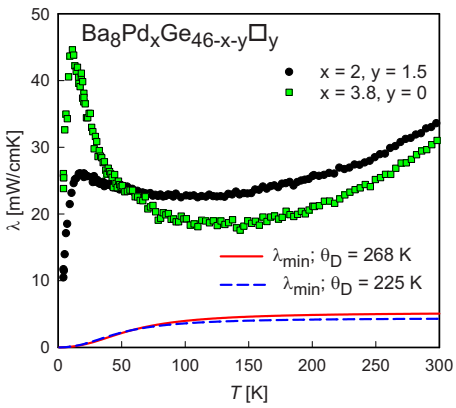

FIG. 12. (Color online) (a) Temperature-dependent thermal conductivity λ of two concentrations of $Ba_8Pd_xGe_{46-x-y}\square_y$.

Analyzing the Hall resistance data R_H in terms of a single-band model based on free electrons—i.e., $R_H=-1/(ne)$ and $\rho=R_H/\mu$ (n is the charge carrier density, e is the electron charge, and μ is the mobility)—we derived the temperature- and field-dependent values of n and μ. Both quantities show only weak dependences on T and B, at least for the phase space investigated. It should be noted that the overall carrier concentration represents an overlay of electrons and holes, dominated by electrons for $x=3.6$.

Measurements performed on other concentrations of the present series were analyzed in a similar manner, revealing the following figures: At $T=10$ K and $\mu_0H=3$ T, n is found to be −3.5, −3.2, −0.83, and 0.56×10^{21} cm^{-3} for $x=2$, 2.9, 3.6, and 3.82, respectively. The mobility μ of these carriers is, respectively, 0.64, 1.6, 0.9, and −0.07 cm^2/(V s). These results refer to electrons as main charge carriers, except for the alloy with $x=3.82$, which appears to be dominated by holes (compare also the thermopower data in Fig. 14). The charge carrier density in the context of the mobility derived for the present series directly renders the sequence of the resistivity data observed. The material with the highest mobility and reasonable charge carrier density was found for $x=2.9$ which, in fact, shows the lowest overall resistivity. The compound with $x=2$ has similar values of n, but the mobility is smaller—hence $\rho(T)$ is larger—in agreement with the experimental data. The largest resistivity is found for $x=3.82$, owing to both small n and small μ values.

A closer inspection of the data (except $x=3.82$) shows that even the system containing the smallest amount of Pd does not behave according to simple metals [compare Fig. 10(b)]. Rather, specific structures of $\rho(T)$ indicate that all the materials investigated are in fact very near to the semiconducting state. The overall behavior resembles both metallicliike and activationlike features as reflected from positive and negative slopes in $\rho(T)$. In order to account for such distinct features, we have developed a model[15] combining the description of simple metals via the Bloch-Grüneisen law with a temperature-dependent charge carrier density. The most relevant assumptions are an electronic DOS represented by a rectangular band and a gap Δ right above the Fermi energy. The charge carrier density is then calculated via standard statistics considering the Fermi-Dirac distribution function.[1,15] Least-squares fits according to this procedure are shown in Fig. 10(b) as solid lines. The principal parameter is the gap width Δ, which increases from about 1000 K for $x=2$ to 2200 K for $x=3.8$. Although the applied model is quite simple, it fairly well describes the temperature-dependent resistivity of $Ba_8Pd_xGe_{46-x-y}\square_y$. The metallic behavior derives from scattering of conduction electrons into unoccupied sites in reciprocal space just above the Fermi energy. Once this region of the DOS becomes occupied, electrons have to be promoted across the gap, originating in semiconducting features. However, a distinct exponential behavior does not become obvious due to the proximity to the metallic state.

The temperature-dependent thermal conductivity λ of $Ba_8Pd_xGe_{46-x-y}\square_y$ is shown for two members of this series in Fig. 12. The overall thermal conductivity values are rather small, expectable for cage-forming compounds which are filled by loosely bound electropositive elements. The increasing Pd content enables a low-temperature maximum to evolve. This distinct feature was observed similarly in clathrates $Ba_8Cd_xGe_{46-x-y}\square_y$ and $Ba_8Zn_xGe_{46-x-y}\square_y$ upon an increasing concentration of Cd or Zn and was associated with the vanishing of vacancies at the 6d sites of the crystal structure. As indicated above no vacancies are found anymore at the 6d sites for $x=3.8$ Pd atoms per unit cell. This infers that scattering of heat carrying phonons is much more intense on vacancies in comparison to the impact of crystallographic disorder originated by the Ge and Pd substitution. Comparing the absolute $\lambda(T)$ values of $Ba_8M_xGe_{46-x-y}\square_y$ with $M=$Zn, Pd, and Cd shows an overall decrease for the sequence Zn, Pd, Cd as a consequence of the growing atomic masses involved. It is interesting to note that none of the samples investigated are characterized by that feature—i.e., a dip in $\lambda(T)$ at lower temperatures—which is attributed to resonance scattering. This mechanism is expected to have a significant impact on thermal transport and is considered responsible for the glasslike behavior in some cage-forming compounds. An archetypal example for the latter is $Eu_8Ga_{16}Ge_{30}$.[17]

A more quantitative description of $\lambda(T)$ is possible in terms of Callaway's theory of lattice thermal conductivity

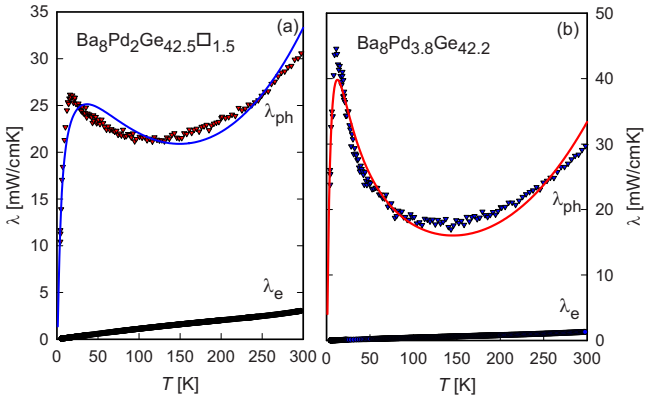

FIG. 13. (Color online) Lattice (λ_{ph}) and electronic (λ_e) thermal conductivity of $Ba_8Pd_2Ge_{42.5}\square_{1.5}$. The solid line is a least-squares fit according to Eq. (3). (b) Lattice (λ_{ph}) and electronic (λ_e) thermal conductivity of $Ba_8Pd_{3.8}Ge_{42.2}$. The solid line is a least-squares fit according to Eq. (3).

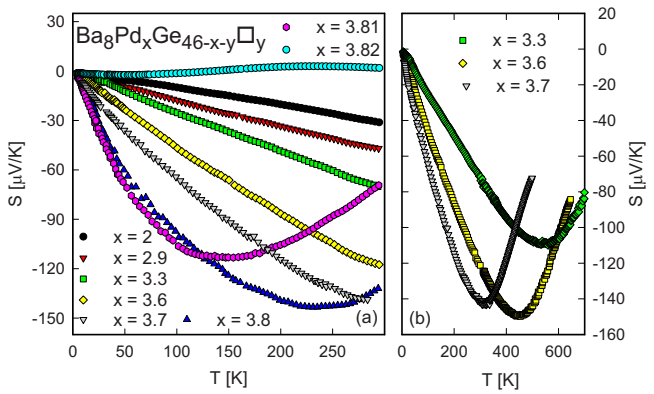

FIG. 14. (Color online) (a) Temperature-dependent thermopower for various concentrations of $Ba_8Pd_xGe_{46-x-y}\square_y$. (b) $S(T)$ of $x=3.3$, $x=3.6$, and $x=3.7$ in an extended temperature range.

λ_{ph}. To derive λ_{ph} from the total thermal conductivity λ, the Wiedemann-Franz law is applied to the $\rho(T)$ data, allowing one to define the electronic thermal conductivity λ_e. Although this model is valid in extended temperature ranges only for free electron systems, it is widely used even for complex materials such as skutterudites or clathrates. The Wiedemann-Franz relation states that increasing electrical resistivities cause decreasing λ_e values. The large overall resistivity of the present samples is thus the cause that λ_e is clearly the minority channel of the total measured effect in both cases [compare Figs. 13(a) and 13(b)].

The temperature dependence of λ_{ph} follows from the basic thermodynamic expression $\lambda=(1/3)C_V v l$, where C_V is the heat capacity of the system, v the particle velocity, and l the mean free path. According to Callaway and von Baeyer,[18] this transforms for the heat-carrying lattice vibrations to

$$\lambda_{ph} = \frac{k_B}{2\pi^2 v_s}\left(\frac{k_B}{\hbar}\right)^3 T^3 \int_0^{\theta_D/T} \frac{\tau_c x^4 e^x}{(e^x-1)^2} dx, \qquad (3)$$

with the velocity of sound, $v_s = \frac{k_B\theta_D}{\hbar(6\pi^2 n)^{1/3}}$, and $x=\hbar\omega/k_BT$, where n is the number of atoms per unit volume and ω the phonon frequency. τ_c^{-1} is the sum of the reciprocal relaxation times for point defect scattering, τ_D^{-1}, umklapp processes, τ_U^{-1}, boundary scattering, τ_B^{-1}, and scattering of phonons by electrons τ_E^{-1}—i.e.,

$$\tau_c^{-1} = \tau_D^{-1} + \tau_U^{-1} + \tau_B^{-1} + \tau_E^{-1}. \qquad (4)$$

Equation (4) does not contain terms for resonance scattering, since they seem to be of minor importance in both compounds studied. In order to get rid of radiation losses, proprietary to the steady-state heat flow method used, a T^3 term was added to Eq. (3) for the analysis.

The initial rise of λ_{ph} may be referred to boundary and point defect scattering; it becomes large when both quantities are small. Note that defects comprise also vacancies. If the strength of umklapp scattering increases, λ_{ph} starts to strongly decrease, thereby forming a maximum at lower temperatures. The latter depends also weakly on the Debye temperature but occurs in general well below $\theta_D/10$. Additionally, an increase of θ_D slightly reduces overall λ_{ph} values. Enhanced scattering of phonons on electrons also efficiently reduces the lattice thermal conductivity.

Least-squares fits according to Eq. (3) are shown in Figs. 13(a) and 13(b) as solid line, revealing only rough agreement with the data observed. A comparison of the sets of fit parameters indicates that the relaxation time referring to point defect scattering—i.e., $\tau_D^{-1}=Dx^4T^4$—with the material-dependent parameter D decreases by more than a factor of 2 when proceeding from the sample with $x=2$ to the sample $x=3.8$. In turn, the strength of the umklapp processes increases simultaneously. The remaining parameters do not show significant changes. These results, which should be used only in a qualitative manner, corroborate the above drawn conclusion that although the disorder due to the Ge and Pd substitution rises, the overall disorder of the crystal decreases at a much stronger rate: this is a consequence of the vacancies vanishing under the growing Pd content.

An approximation according to Cahill and Pohl,[19] allows us to estimate the theoretical lower limit of the lattice thermal conductivity, which primarily is defined by the number N of atoms per unit volume and by the Debye temperature. Taking $N=4.32\times10^{22}$ cm^{-3} and $\theta_D=225$ K for $Ba_8Pd_2Ge_{42.5}\square_{1.5}$ reveals $\lambda_{min}(300\text{ K})=4.3$ mW/(cm K). A slightly larger value of 5.1 mW/(cm K) is derived taking $\theta_D=268$ K, obtained from the low-temperature extrapolation of the heat capacity data. Results below room temperature are shown in Fig. 12 as dashed and solid lines for both sets of parameters.

Results regarding the temperature-dependent thermopower S are plotted in Figs. 14(a) and 14(b) for various concentrations of $Ba_8Pd_xGe_{46-x-y}\square_y$. $S(T)$ is characterized by a Pd-dependent evolution of the absolute $S(T)$ values up to about $x=3.8$. Within this concentration range $S(T)$ is negative, referring to electrons as the principal charge carriers. In contrast, $S(T)$ becomes positive for $x=3.82$, indicative of holes as majority charge carriers. The compound with $x=3.8$ exhibits thermopower values up to -145 μV/K, well below room temperature, and thus belongs to those members

of clathrates having the largest $S(T)$ values. The almost linear temperature dependence of $S(T)$, except those compounds with very large Pd concentrations, suggests a simple origin, depending primarily on the charge carrier density n. As demonstrated, e.g., in Ref. 20, the diffusion part of the thermopower can simply be represented by

$$S_d = \frac{\pi^2 k_B^2 2m_e}{e\hbar^2(3n\pi^2)^{2/3}}T, \tag{5}$$

where m_e is the mass of the carriers and e is the respective charge. Approaching the data of Fig. 14 by a linear dependence, at least for concentrations from $x=2$ up to $x=3.6$, and $T<350$ to 400 K allows to calculate the charge carrier density [Eq. (5)], which decreases almost by one order of magnitude from $n=2.9\times10^{21}$ cm^{-3} for $x=2$ to $n=3.4\times10^{20}$ cm^{-3} for $x=3.6$. These figures are in perfect agreement to the above indicated Hall data. A further justification for such an estimation of n from thermopower data regarding type-I clathrate systems was obtained previously from measurements of the optical conductivity in $Ba_8Zn_xGe_{46-x-y}\square_y$ compounds, where n deduced from the plasma frequency excellently agreed with an estimation of n based on Eq. (5).

Figure 14(b) demonstrates that the almost linear dependence of $S(T)$ is restricted to lower, concentration-dependent temperatures. Above the nearly linear dependence, a minimum develops, followed by a decrease of $|S(T)|$. A possible explanation of this observation may follow from the concentration-dependent gap in the electronic density of states above E_F: Once thermal energy is sufficient to appreciably populate the states above the gap, the number of charge carriers increases accordingly [compare Eq. (5)] and $|S(T)|$ becomes reduced.

IV. SUMMARY

Starting from binary $Ba_8Ge_{43}\square_3$ a series of clathrates was synthesized forming a solid solution $Ba_8Pd_xGe_{46-x-y}\square_y$, with a solubility limit of 3.8 Pd atoms per formula unit at 800 °C. Throughout the homogeneity region cubic primitive symmetry consistent with the type-I clathrate has been confirmed. Phase relations at subsolidus temperatures and at 800 °C as well as the primary field of clathrate crystallization were derived.

Physical properties such as charge carrier density and transport quantities were found to be heavily influenced by Ge/Pd substitution in the clathrate framework: the system changes from a bad metal for lower Pd content to a clear activation-type behavior for the largest Pd concentration. This gradual change is originated by the combined effect of both the substitution of Ge by Pd and by the vanishing of vacancies. Thermopower indicates that the majority charge carriers are electrons, but the density of these carriers decreases by almost one order of magnitude when proceeding from a Pd content $x=2$ to $x=3.8$. The observation that the sample with $x=2$ has a larger overall resistivity than that with $x=2.9$, although the charge carrier density is already reduced, is then associated with an improved mobility of the charge carriers in the latter case as a consequence of a reduced number of vacancies. The efficiency of scattering on such vacancies is evidenced also from the thermal conductivity study.

A simple model of the electronic density of states, constituted by a narrow gap right above the Fermi energy, allowed us to qualitatively account for details of the temperature-dependent electrical resistivity. Thermal conductivity data are modeled in terms of Callaway's theory of heat-carrying phonons. Specific heat measurements and inelastic neutron spectroscopy identified low-energy optical modes, which are characterized by a correlated movement of the Ba(2) filler and the Pd and Ge framework atoms.

Measurements of the Seebeck coefficient allowed a rough estimation of the charge carrier density and the nature of the carriers. Additionally, $S(T)$ basically defines the figure of merit $ZT=S^2T/(\rho\lambda)$, which represents the thermoelectric performance of a certain material. Using the compound with the highest Seebeck coefficient—i.e., $x=3.8$—reveals $ZT=0.045$ at 250 K. Technical applications become of interest if ZT approaches roughly a value of the order of 1, as realized in Bi_2Te_3 with $ZT(300\text{ K})\approx0.7$.

ACKNOWLEDGMENTS

The research reported herein was sponsored by the Austrian FWF Projects Nos. P16370, P19165, and P16778-No2 and supported by the EU network of excellence CMA ("Complex Metallic Alloys," Contract No. NMP3-CT-2005-500140). N.M-K. and P.R. are both grateful to the OEAD Austrian—Ukrainian Scientific—Technological Exchange Program in Vienna.

[1] N. Melnychenko-Koblyuk, A. Grytsiv, S. Berger, H. Kaldarar, H. Michor, F. Röhrbacher, E. Royanian, E. Bauer, P. Rogl, H. Schmid, and G. Giester, J. Phys.: Condens. Matter **19**, 046203 (2007).

[2] N. Melnychenkc-Koblyuk, A. Grytsiv, L. Fornasari, H. Kaldarar, H. Michor, F. Röhrbacher, M. Koza, E. Royanian, E. Bauer, P. Rogl, M. Rotter, H. Schmid, F. Marabelli, A. Devishvili, M. Doerr, and G. Giester, J. Phys.: Condens. Matter **19**, 216223 (2007).

[3] W. Carrillo-Cabrera, J. Curda, K. Petters, M. Baenitz, Y. Grin, and von H. G. Schnering, Z. Kristallogr. **215**, 321 (2000).

[4] W. Carrillo-Cabrera, S. Budnyk, Y. Prots, and Y. Grin, Z. Anorg. Allg. Chem. **630**, 7226 (2004).

[5] G. Cordier and P. Woll, J. Less-Common Met. **169**, 291 (1991).

[6] W. Carrillo-Cabrera, H. Borrmann, S. Paschen, M. Baenitz, F. Steglich, and Y. Grin, J. Solid State Chem. **178**, 715 (2005).

[7] L. J. van der Pauw, Philips Tech. Rev. **26**, 220 (1958/1959).

[8] National Institute of Standards and Technology, www.eeel.nist.gov/812/hall.html

[9] N. Melnychenko-Koblyuk, A. Grytsiv, E. Bauer, P. Rogl, H.

Schmid, and G. Giester (unpublished).
[10] T. B. Massalski, *Binary Alloy Phase Diagrams*, 2nd ed. (ASM International, Metals Park, OH, 1990).
[11] E. Parthé, L. Gelato, B. Chabot, M. Penzo, K. Cenzual, and R. Gladyshevskii, *TYPIX—Standardized Data and Crystal Chemical Characterization of Inorganic Structure Types* (Springer-Verlag, Berlin, 1994).
[12] A. Czybulka, B. Kuhl, and H. U. Schuster, Z. Anorg. Allg. Chem. **594**, 23 (1991).
[13] A. Junod, D. Bichsel, and J. Mueller, Helv. Phys. Acta **52**, 580 (1979).
[14] A. Junod, T. Jarlborg, and J. Müller, Phys. Rev. B **27**, 1568 (1983).
[15] St. Berger, Ph.D thesis, Vienna University of Technology, 2003.
[16] N. W. Ashcroft and N. D. Mermin, *Festköperphysik* (Oldenburg, München, 2005).
[17] J. L. Cohn, G. S. Nolas, V. Fessatidis, T. H. Metcalf, and G. A. Slack, Phys. Rev. Lett. **82**, 779 (1999).
[18] J. Callaway and H. C. von Baeyer, Phys. Rev. **120**, 1149 (1960).
[19] D. Cahill and R. Pohl, Solid State Commun. **70**, 927 (1989).
[20] S. Paschen, V. H. Tran, M. Baenitz, W. Carrillo-Cabrera, Y. Grin, and F. Steglich, Phys. Rev. B **65**, 134435 (2002).